frontiers | Frontiers in Earth Science

TYPE Original Research
PUBLISHED 25 August 2022
DOI 10.3389/feart.2022.993796

OPEN ACCESS

EDITED BY
Wenjun Zheng,
School of Earth Sciences and Engineering, Sun Yat-sen University, China

REVIEWED BY
Liang Qiu,
China University of Geosciences, China
Jingen Dai,
China University of Geosciences, China
Zhikun Ren,
Institute of Geology, China Earthquake Administration, China

*CORRESPONDENCE
Xiaoming Shen,
xiaoming_shen@163.com

SPECIALTY SECTION
This article was submitted to Structural Geology and Tectonics, a section of the journal Frontiers in Earth Science

RECEIVED 14 July 2022
ACCEPTED 04 August 2022
PUBLISHED 25 August 2022

CITATION
Wang S, Shen X, Chevalier M-L, Replumaz A, Zheng Y, Li H, Pan J, Li K and Xu X (2022), Illite K-Ar and (U-Th)/He low-temperature thermochronology reveal onset timing of Yadong-Gulu rift in southern Tibetan Plateau.
Front. Earth Sci. 10:993796.
doi: 10.3389/feart.2022.993796

Illite K-Ar and (U-Th)/He low-temperature thermochronology reveal onset timing of Yadong-Gulu rift in southern Tibetan Plateau

Shiguang Wang[1,2], Xiaoming Shen[1]*, Marie-Luce Chevalier[3,4,5], Anne Replumaz[6], Yong Zheng[3,4,5], Haibing Li[3,4,5], Jiawei Pan[3,4,5], Kang Li[1] Xiwei Xu[1]

[1]National Institute of Natural Hazards, Ministry of Emergency Management of China, Beijing, China, [2]Institute of Geophysics, China Earthquake Administration, Beijing, China, [3]Southern Marine Science and Engineering Guangdong Laboratory (Guangzhou), Guangzhou, China, [4]Key Laboratory of Deep-Earth Dynamics of Ministry of Natural Resources, Institute of Geology, Chinese Academy of Geological Sciences, Beijing, China, [5]Jiangsu Donghai Crustal Activity in Deep Holes of the Continental Scientific Drilling National Observation and Research Station, Lianyungang, China, [6]School of Earth and Space Sciences, ISTerre, Université Grenoble Alpes, National Center for Scientific Research, Grenoble, France

Determining the timing of E-W extension across the NS-trending rifts in southern Tibet is key to test the mechanical models of the latest evolution in the collision between India and Asia. We focus on the southern half of the largest of the seven main rifts, the Yadong-Gulu rift (YGR), which, despite being the focus of numerous studies thanks to its easy access, still lacks direct time constraints. Using illite K-Ar ages of fault gouge from the active Yadong normal fault of the YGR, we directly constrain its onset timing at 9 ± 1 Ma. (U-Th)/He dating of the footwall leucogranite reveals a rapid exhumation of the southern YGR since ~9 Ma, attesting to its onset activity. Such timing is similar to that estimated for the northern half of the YGR at 8 ± 1 Ma, suggesting that the entire YGR formed at approximately the same time. Our synthesis of published initiation ages of the other main rifts in southern Tibet shows that they mostly fall between ~23 and 8 Ma, suggesting a clear spatial and temporal pattern of old initiation ages to the west and young to the east. In this case, the formation of rifts in southern Tibet is unlikely caused by slab tearing of the underthruting Indian plate or orogenic collapse. Our study supports that E-W extension in Tibetan Plateau is triggered by a combination of eastward propagation of the Karakorum-Jiali fault zone and divergent thrusting along the curved Himalayan arc.

KEYWORDS

Southern Tibetan Plateau, illite K-Ar, low-temperature thermochronology, Yadong-Gulu rift, onset timing

Introduction

The Tibetan Plateau, resulting from the continent-continent collision of the Indian and Asian plates, shows an emblematic paradox that, despite ongoing ~N-S shortening between the Tibetan Plateau and the Indian plate, the latest deformation is dominated by ~E-W extension in southern Tibet (e.g., Tapponnier et al., 1981; Armijo et al., 1986; Coleman and Hodges 1995; Chevalier et al., 2020). Indeed, seven main, parallel ~NS-trending rifts, resulting from E-W extension, attest to the latest and strongest tectonic activity in the southern half of the plateau (Figures 1A,B). Two main models have been proposed to explain the rifts formation. On one hand, one type of model focuses on lithospheric dynamics, in which either orogenic collapse (Dewey, 1988), delamination of thickened mantle lithosphere (England and Houseman, 1989), eastward flow of low-viscosity lower crust (Royden et al., 1997; Yin and Taylor, 2011), or tearing of subducting Indian lithospheric slab (Chen et al., 2015; Bian et al., 2020) is regarded as the main mechanism. On the other hand, another type of model emphasizes the boundary forces and regional stress fields. In such case, the rifts open either as pull-apart basins at the end of strike-slip faults accommodating the eastward extrusion of Tibet (Tapponnier et al., 1982; Armijo et al., 1986), northward propagation of underthrusting Indian slab (DeCelles et al., 2002), inward bending of orogen rims (Kllotwijk et al., 1985), or basal shear from oblique underthrusting of the Indian plate (McCaffery and Nabelek, 1998).

Although numerous studies have documented the initiation age of the south Tibetan rifts to test these models, the ages are spread out, ranging from ~23 to 2 Ma (Figure 1C; Supplementary Table S1, and references therein), partly due to the different dating methods used, thus resulting in a hot debate on the dynamic mechanisms responsible for the rifts' formation. For example, Bian et al. (2022) suggested that the Yadong-Gulu rift (YGR) initiated at ~13–11 Ma based on apatite fission track and (U-Th)/He dating. They further proposed that the onset timing of the YGR is younging northward, due to outward expansion of the Himalayan arc. Using (U-Th)/He thermochronology, Sundell et al. (2013) determined initiation ages for the South Lunggar rifts to be >10 Ma with a rifting acceleration at 5–2 Ma, which they explained was caused by a combination of gravitional orogenic collapse and underthrusting Indian lithosphere. Therefore, the exact determination of the rifts' onset timing and their spatio-temporal variations are of great importance for the analysis of the E-W extension dynamics in southern Tibetan Plateau.

Previous studies usually used low-temperature (U-Th)/He or fission-track thermochronology of pluton or basin sediments in the rifts to indirectly determine their initiation timing (e.g., Mahéo et al., 2007; Styron et al., 2013; Sundell et al., 2013; McCallister et al., 2014; Shen et al., 2016; Bian et al., 2020, 2022; Shen et al.,. 2022a). In recent years, thanks to the advances in low-temperature dating techniques, fault gouge dating has also been used to offer direct information on the timing of faulting events (e.g., Van der Pluijm et al., 2001; Duvall et al., 2011; Zheng et al., 2016). In this paper, we use illite K-Ar dating of fault gouge, as well as zircon U-Pb, and zircon and apatite (U-Th)/He thermochronology of leucogranite from the footwall of the active Yadong normal fault to determine the onset timing of the southern YGR. We further reconstruct the thermal history and activity of the YGR and discuss the spatio-temporal pattern and dynamics of E-W extension in southern Tibet.

Geological setting

The YGR consists of several Neogene-Quaternary fill basins and NNE-NE-trending bounding normal faults. It is the longest (~500 km) and most prominent rift in southern Tibet, extending from Yadong in the Himalayas to north of Gulu in the Lhasa terrane. It cuts across the Himalayan terrane, South Tibetan Detachment System (STDS), Yarlung Zangbo suture, and Lhasa terrane (Figure 1B). It is bounded to the north and south by the Karakorum-Jiali fault zone (KJFZ) and Main Frontal Thrust (MFT), respectively (Figure 1A; e.g., Armijo et al., 1986; Chevalier et al., 2020; Wang et al., 2020). The YGR is also the most active rift in southern Tibet, with 14 M≥6.0 earthquakes since 1264 A.D. (Wu et al., 2011), as well as significant hydrothermal activity. In view of the geometry of the bounding faults, Armijo et al. (1986) divided the YGR into three sections: northern, central, and southern section, with a total of seven grabens or half-grabens. In the south, the Yadong rift runs from Yadong town to the Yarlung Zangbo suture (YZS), and is characterized by W-dipping normal faults along three right-stepping en-echelon grabens (Pagri, Nierudui, and Relong from south to north). In the center, from the YZS to Yangbajing town, the Angang and Yangbajing grabens are bounded by nearly symmetrical normal faults dipping to the west and east. By contrast, while the northern section from Yangbajing to the Gulu bend is bounded by faults with both left-lateral and normal components along the SE side of the Nyainqentanglha mountain range, only a large normal fault exists north of the Gulu bend.

Our study area is located in the ~130 km-long, ~20 km-wide Pagri graben, southernmost Yadong rift (Figure 2A). Boundary normal faults in this graben dip to the W-NW at an angle of 50°–70° (Figures 3H, 4H; Wang et al., 2020), cutting and offsetting the ~EW-trending South Tibetan Detachment System (STDS) (Wu et al., 1998; Dong et al., 2021). Field evidence showed rapid normal faulting along the Pagri graben in the Quaternary, with, for example, >2.6 km of topographic relief (Armijo et al., 1986), and <17 ± 1 m offset since the global Last Glacial Maximum (~20 ka) (Wang et al., 2020; Chevalier et al., 2022). Additional evidence such as earthquake-triggered landslide at 13–15 ka (Peng et al., 2018), as well as fresh surface rupture and hot springs (Wang et al., 2020) are also present. The

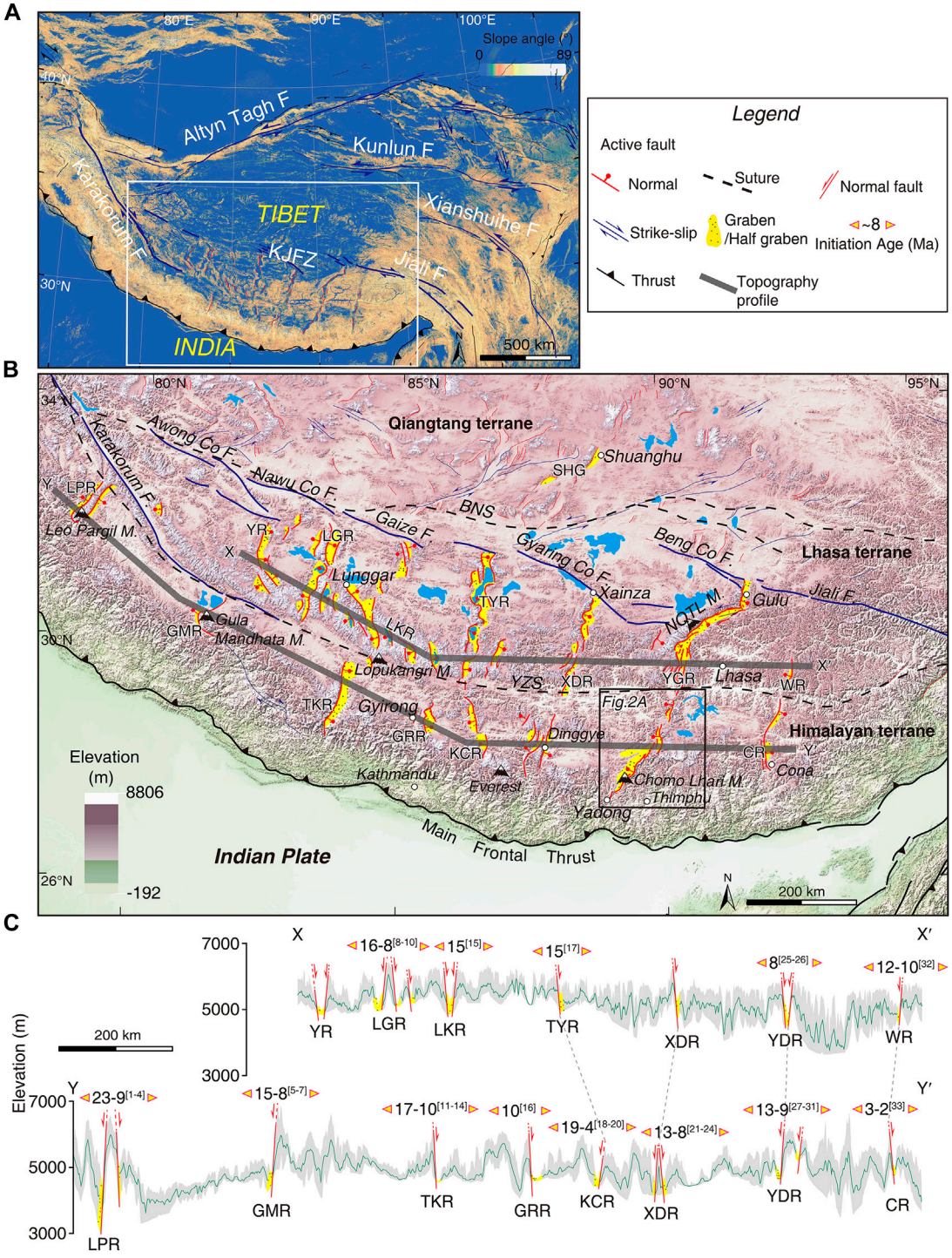

FIGURE 1
(A) Slope map and main active faults of Tibetan Plateau. **(B)** Active faults of Tibetan Plateau interior with main rifts, modified from Tapponnier et al. (2001) and Chevalier et al. (2020) **(C)** Topographic profiles across the south Tibetan rifts with initiation ages in Ma (references as in Supplementary Table S1). Main rifts and sutures are: CR, Cona rift; GMR, Gurla Mandhata rift; GRR, Gyirong rift; KCR, Kung Co rift; LGR, Lunggar rift; LPR, Leo Pargil rift; SHG, Shuanghu graben; TKR, Thakkhola rift; TYR, Tangra Yumco rift; WR, Woka rift; XDR, Xainza-Dinggye rift; YGR, Yadong-Gulu rift; YR, Yari rift; NQTL, Nyainqentanglha; KJFZ, Karakorum-Jiali fault zone; BNS, Bangong-Nujiang suture; YZS, Yarlung Zangbo suture.

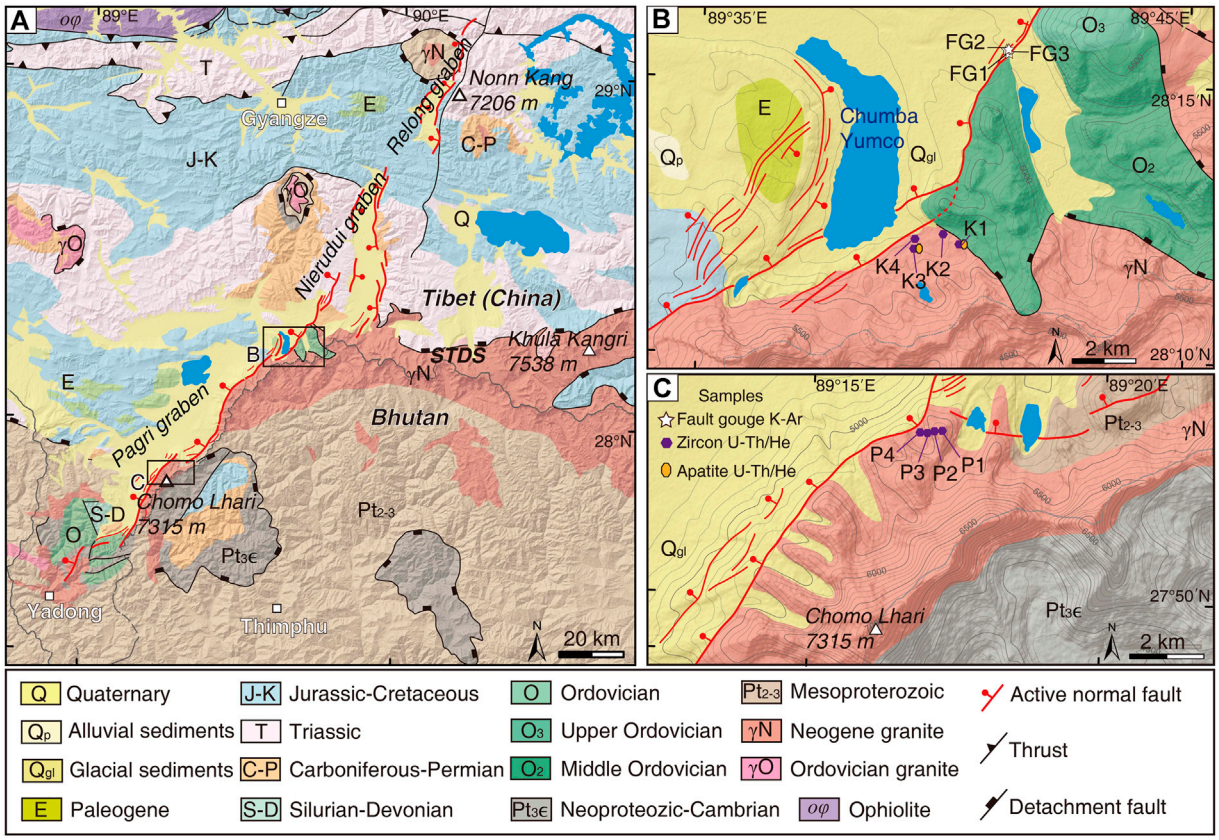

FIGURE 2
(A) Geological map of the southern YGR (location in Figure 1B) [revised from China University of Geosciences (Beijing) (CUGB), 2004]. **(B)** Geological map of Chumba Yumco area with sample locations (FG1–FG3, K1–K4) (location in A). **(C)** Geological map of Chomo Lhari area with sample locations (P1–P4) (location in A). STDS-South Tibetan Detachment System.

hanging wall of the active Yadong normal fault consists of Holocene and Pleistocene conglomerate, as well as Paleogene conglomerate and sandstone. The footwall is composed of Cenozoic leucogranite, Paleozoic limestone, and intensely deformed Proterozoic metamorphic rocks such as gneiss and schist (Figure 2). Mesozoic strata including sandstone, limestone, and slate are underlying the Quaternary deposits to the north and overlie on top of Proterozoic metamorphic rocks to the south (Figure 2).

Field observation and sampling strategy

Cenozoic leucogranite is uplifted in the footwall of the YGR along the rugged NE-trending Chomo Lhari Range (Figure 2A). About 6 km north of Chomo Lhari peak (7,315 m), a series of triangular facets, with ~400–600 m relief (Figure 3A), lie at the foot of the mountain range. Active normal faults dipping to the NW at a high angle of 60°–70° (Figures 3C,H, 4H) separate the leucogranite in the footwall from Pleistocene conglomerate in the hanging wall. We collected four leucogranite samples (P1–P4, Figures 2C, Figures 3A–G locations in Table 1) along a vertical transect on one of the triangular facets at altitudes ranging from 5,350 to 5,700 m (Figures 3D,E) for zircon U-Pb (P1) and (U-Th)/He dating (P1-P4). Just SE of Chumba Yumco Lake, the active, NW-dipping normal faults (at a high angle of 65°–75°) (Figure 4H) offset the STDS (Figure 2A), leucogranite, and Pleistocene-Holocene conglomerate. We also collected four similar samples (K1–K4; Figures 2B, Figures 4A–G, locations in Table 1) in the footwall's leucogranite for zircon U-Pb (sample K3) and (U-Th)/He dating between altitudes of 4,560 and 4,770 m (Figures 4B,C).

Northeast of Chumba Yumco, ~6 km north of samples K1–K4, active normal faults strike NE, dip at ~50° to the NW, and offset Holocene travertine deposits resulting in fresh ruptures considered as paleoearthquake relics (Zuo et al., 2021; Figures 5A–C). The footwall is made of Ordovician limestone where at least four different fault branches offset the Holocene travertine and conglomerate deposits made of

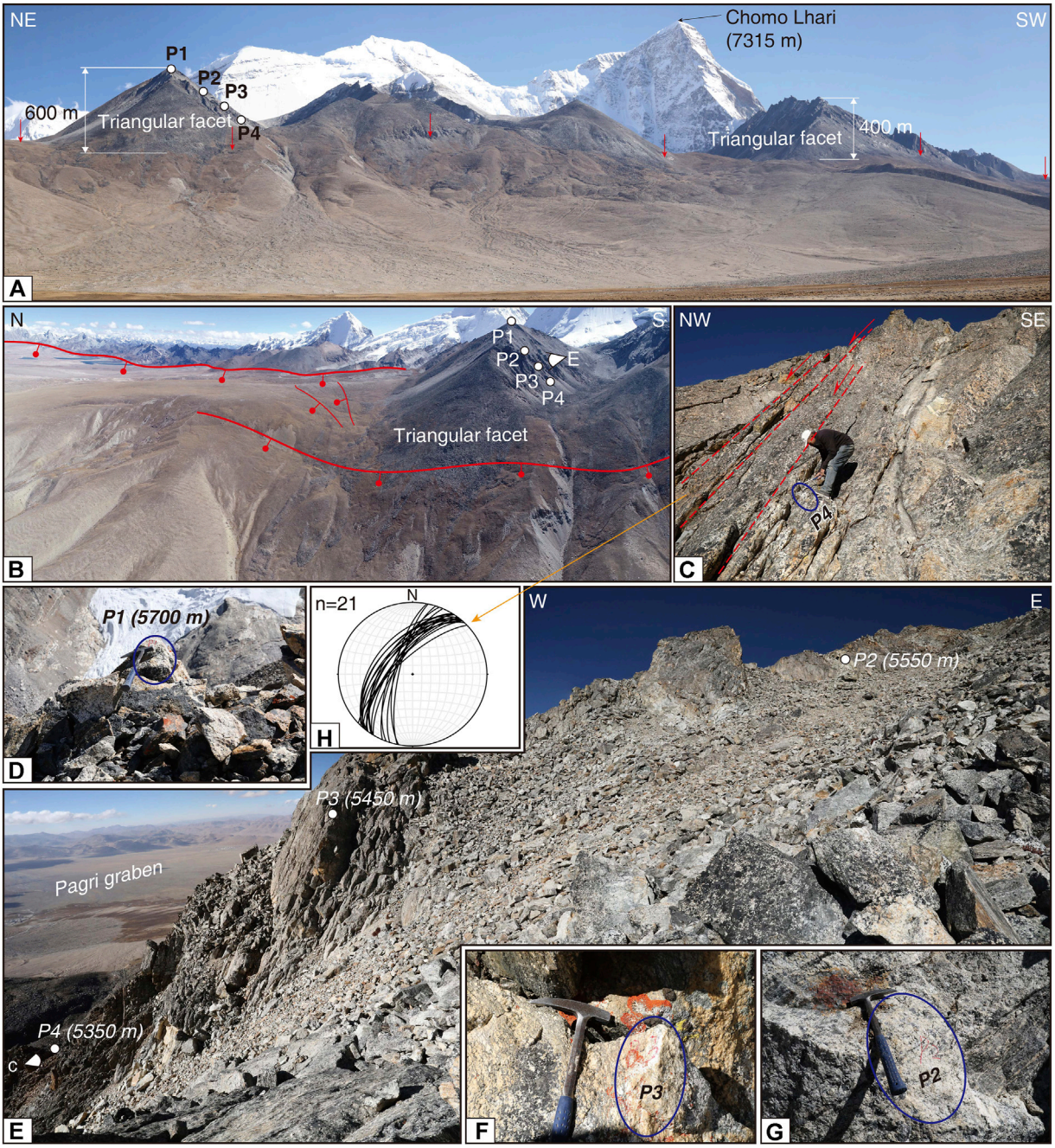

FIGURE 3
Field photos of active normal faults north of Chomo Lhari Mountain along southernmost YGR and location of samples P1–P4. **(A)** Triangular facets along YGR active normal faults and location of samples P1–P4. Red arrow refers to the active Yadong normal fault. Note Chomo Lhari peak (7,315 m) in the background. **(B)** Unmanned aerial vehicle (UAV) photo of samples P1–P4 and active normal faults. **(C)** Outcrop of sample P4 and brittle normal fault. **(D–G)** Outcrop and location with elevations of samples P1 (5,700 m), P2 (5,550 m), P3 (5,450 m), and P4 (5,350 m). **(H)** Foliations in the YGR normal fault north of Chomo Lhari Mountain, indicating the high-angle of active normal fault.

~50 m of cataclastic rocks and ~120 m of fault gouge/breccia zone (Figure 5A). Below the travertine, along the fault plane, the outcrop reveals two ~1 m-wide fresh black fault gouge layers (Figures 5B–F), which can be used to obtain direct constraints for the onset timing of normal faulting (e.g., Duvall et al., 2011; Mottram et al., 2020). The black fault gouge is slightly foliated and half-consolidated with a few calcite veins. Within the strong foliated black fault gouge layers, we collected three clay-rich

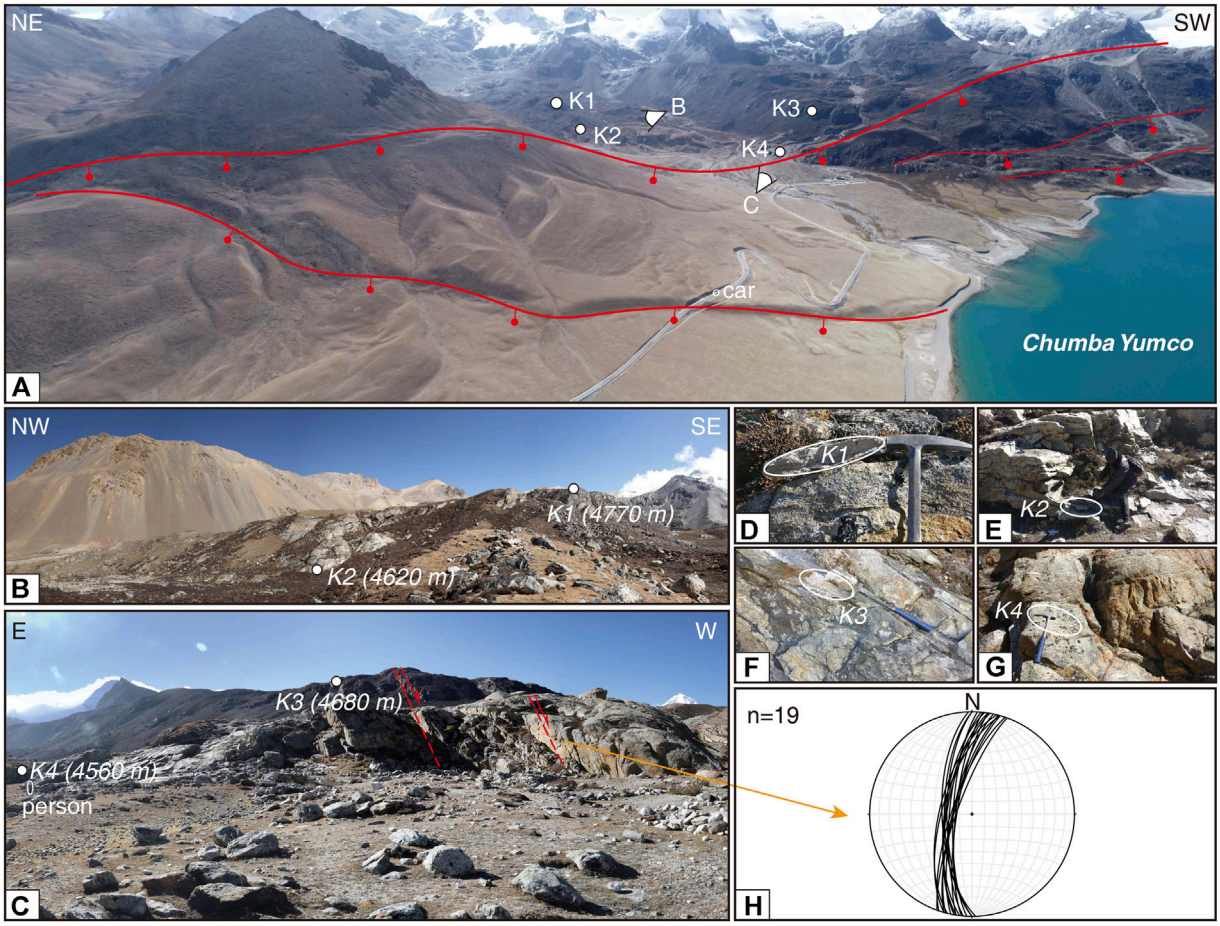

FIGURE 4
Field photos of active Yadong normal faults south of Chumba Yumco lake. **(A)** UAV photo of active faults south of the lake and location of samples K1–K4. **(B,C)** Location of samples K1 (4,770 m), K2 (4,620 m) K3 (4,680 m), and K4 (4,560 m). **(D–G)** Outcrops of samples K1–K4. **(H)** Foliations in the YGR normal fault south of Chumba Yumco lake, indicating the high-angle of active normal fault.

samples for K-Ar dating (FG1–FG3, Figures 5D,F), located next to a ~2 m-high waterfall, most likely resulting from the last large earthquake, which offset the active river (Figures 5A,B) (Wang et al., 2020).

Materials and methods

In order to reveal the exhumation history of the YGR, clay mineral illite K-Ar dating was used to date the fault gouge samples (FG1–FG3), i.e., to date the onset timing of the active, bounding normal faults of the southern YGR. Low-temperature zircon and apatite (U-Th)/He thermochronology, as well as high-temperature zircon U-Pb dating were also applied to the leucogranite samples (K1–K4 and P1–P4) to constrain the activity timing of the YGR.

Fault gouge authigenic illite K-Ar dating

$2M_1$ and $1M_d$ polytypes of illite usually coexist in fault gouge, which is generated in a shallow brittle fault zone in nature (Van der Pluijm et al., 2001; Duvall et al., 2011). The former $2M_1$ phase, which is a more stable phase that forms above 280°C (Velde, 1965), is usually derived from the surrounding wall rocks, whereas the latter $1M_d$ polytype is also referred to as the authigenic illite that usually grows below 200°C in fault gouge (Haines and Van der Pluijm, 2010; Duvall et al., 2011). Due to the ratio of fine size authigenic illite (<2 μm) and $2M_1$ polytype illite becoming higher in finer grain size, the authigenic illite age, representing the active timing of brittle faults, is normally determined by plotting K-Ar ages versus wall rocks-derived illite percentages in various sizes of isolating illite. The fitting line intercept with 0% and 100% of detrital ($2M_1$) illite end

TABLE 1 Single-grain zircon an apatite (U-Th)/He results from Leucogranite along southern section of YGR.

Sample	^{4}He	^{238}U	^{232}Th	Raw age	Error	Rs	FT	Corrected	Error	Mean age	eU
No.	(mol)	(ppm)	(ppm)	(Ma)	(±1σ)	(μm)		age (Ma)	(±1σ)	(±1σ) (Ma)	(ppm)
Zircon (U-Th)/He results											
P1, 89.286366°E, 27.876033°N, 5,700 m											
Z1	6.01E-13	1,421.52	67.66	11.25	0.21	55.33	0.78	11.25	0.21	11.22 ± 1.42	1,437.4
Z2	1.14E-12	2,567.19	55.65	13.13	0.23	52.13	0.77	13.13	0.23		2,580.3
Z3	2.18E-13	1,112.59	96.36	9.77	0.18	45.84	0.74	9.77	0.18		1,135.2
Z4	6.04E-13	1,022.07	86.42	10.72	0.18	52.16	0.77	10.72	0.18		1,042.4
P2, 89.286629°E, 27.872261°N, 5,550 m											
Z1	3.17E-13	614.23	112.43	10.17	0.19	61.46	0.80	10.17	0.19	10.46 ± 1.04	640.7
Z2	7.90E-13	1,098.25	80.81	11.48	0.21	66.34	0.81	11.48	0.21		1,117.2
Z3	4.48E-13	676.56	427.91	9.13	0.22	65.21	0.80	9.13	0.22		777.1
Z4	3.28E-13	410.08	246.19	11.07	0.19	67.28	0.81	11.07	0.19		467.9
P3,89.285261°E, 27.871767°N, 5,450 m											
Z1	3.12E-13	801.313	63.646	10.13	0.51	53.19	0.77	10.13	0.51	10.88 ± 0.65	816.3
Z2	9.77E-13	778.217	96.039	25.93	0.46	57.83	0.79	25.93	0.46		800.8
Z3	5.16E-13	830.741	121.41	11.31	0.20	59.01	0.79	11.31	0.20		859.3
Z4	9.37E-13	1,408.36	61.468	11.20	0.21	62.55	0.80	11.20	0.21		1,422.8
P4, 89.283822°E, 27.871983°N, 5,350 m											
Z1	1.45E-13	540.16	62.86	9.55	0.17	49.11	0.75	9.55	0.17	9.58 ± 0.05	554.9
Z2	1.17E-13	585.72	84.75	9.56	0.16	45.63	0.73	9.56	0.16		605.6
Z3	2.15E-13	786.54	56.77	9.54	0.17	50.24	0.76	9.54	0.17		799.9
Z4	1.50E-13	701.95	90.56	9.66	0.18	45.77	0.73	9.66	0.18		723.2
K1, 89.672762°E, 28.200880°N, 4,770 m											
Z1	1.49E-12	1,495.59	66.93	8.72	0.17	74.60	0.83	8.72	0.17	8.78 ± 1.54	1,511.3
Z2	6.73E-13	1,323.91	66.93	10.95	0.20	57.54	0.79	10.95	0.20		1,339.6
Z3	5.57E-13	1,535.88	73.87	8.04	0.14	54.48	0.78	8.04	0.14		1,553.2
Z4	4.25E-13	2,249.98	179.40	7.42	0.13	47.15	0.74	7.42	0.13		2,292.1
K2, 89.667226°E, 28.203987°N, 4,620 m											
Z1	1.61E-13	873.28	87.24	5.62	0.09	50.53	0.76	5.62	0.09	7.97 ± 1.61	893.8
Z2	4.28E-13	1767.31	242.05	8.80	0.16	46.82	0.74	8.80	0.16		1824.2
Z3	2.63E-13	965.07	137.37	8.32	0.16	51.63	0.76	8.32	0.16		997.3
Z4	3.94E-13	1906.24	315.52	9.16	0.18	46.44	0.74	9.16	0.18		1980.4
K3, 89.657206°E, 28.199202°N, 4,680 m											
Z1	1.23E-12	1743.07	107.02	10.07	0.21	66.09	0.81	10.07	0.21	8.61 ± 1.08	1,768.2
Z2	4.49E-13	1,072.65	92.66	8.61	0.15	57.26	0.79	8.61	0.15		1,094.4
Z3	1.45E-13	513.18	120.94	7.49	0.14	54.37	0.77	7.49	0.14		541.6
Z4	2.85E-13	734.91	175.30	8.29	0.16	53.34	0.77	8.29	0.16		776.1
K4, 89.657435°E, 28.202538°N, 4,560 m											
Z1	3.35E-13	1,033.40	322.28	8.09	0.14	52.18	0.76	8.09	0.14	7.8 ± 0.43	1,109.1
Z2	2.17E-13	922.67	229.08	7.74	0.14	51.58	0.76	7.74	0.14		976.5
Z3	1.75E-13	1,136.33	164.91	7.21	0.12	44.67	0.73	7.21	0.12		1,175.1
Z4	1.66E-13	1,091.44	297.83	8.14	0.14	44.38	0.72	8.14	0.14		1,161.4
Apatite (U-Th)/He results											
K1, 89.672762°E, 28.200880°N, 4,770 m											
A1	1.20E-11	1,515.86	56.06	5.1	0.11	47.36	0.62	8.22	0.18	8.71 ± 0.7	1,529.0

(Continued on following page)

TABLE 1 (*Continued*) Single-grain zircon an apatite (U-Th)/He results from Leucogranite along southern section of YGR.

Sample	^{4}He	^{238}U	^{232}Th	Raw age	Error	Rs	FT	Corrected	Error	Mean age	eU
No.	(mol)	(ppm)	(ppm)	(Ma)	(±1σ)	(μm)		age (Ma)	(±1σ)	(±1σ) (Ma)	(ppm)
A2	2.61E-13	14.22	1.90	6.51	0.16	61.59	0.71	9.21	0.23		14.7
K3, 89.657206°E, 28.199202°N, 4,680 m											
A1	4.08E-13	53.62	5.01	5.13	0.12	46.61	0.61	8.36	0.20	8.53 ± 0.24	54.8
A2	7.60E-13	105.12	7.90	5.27	0.12	45.7	0.61	8.69	0.20		107.0

Rs, Radius of a sphere with the equivalent surface area-to-volume ratio as cylindrical crystals Meesters and Dunai (2002). Ft: α-ejection correction factor Farley et al. (1996). Mean age: Weighted means calculated using IsoplotR Vermeesch (2018). Clear older age outliers are highlighted in bold and are excluded from calculation of the weighted mean age. eU, Effective uranium content, [eU] = [U] + 0.235 × [Th] Flowers et al. (2009). Shaded data are outliers

members represents the fault-related authigenic illite age and wall rock-derived detrital illite age, respectively (Van der Pluijm et al., 2001; Yamasaki et al., 2013).

Illite isolation was carried out at the Institute of Geology, Chinese Academy of Geological Sciences, Beijing, following the detailed procedures of Zheng et al. (2014, 2016). Using gravitational floating in deionized water and ultra-centrifugation separation methods, fault gouge samples FG2 and FG3 were subdivided into four grain size fractions: 1–2, 0.5–1, 0.25–0.5, and 0.25 μm, while FG1 was subdivided into three size fractions (no 0.5–1 μm). These aliquots were characterized by X-ray diffraction (XRD) to determine the content of illites at the Institute of Geology and Geophysics, Chinese Academy of Sciences, Beijing. Quantification of the $2M_1$ and $1M_d$ polytypes of illite was calculated by the BGMN software (Bergmann et al., 1998; Ufer et al., 2012). Then, each fraction was analyzed by K-Ar analytical method at the Analytical Laboratory of Beijing Research Institute of Uranium Geology, following the detailed methods of Zwingmann and Mancktelow (2004). K-Ar ages and errors <1% (2σ) were calculated based on the K and radiogenic ^{40}Ar concentrations with the usual decay constants (Steiger and Jäger, 1977).

Zircon U-Pb method

Zircon crystals were selected at the Langfang Regional Geological Survey, China, by combining magnetic and heavy liquid separation techniques from whole-rock samples. Under a binocular microscope, well-shaped zircons without inclusions, cracks and corrosion were handpicked. All zircons were photographed using MIRA 3 scanning electron microscope and cathodoluminescence (CL) (Supplementary Figure S1) to document their internal structures. Zircon U–Pb dating was obtained by laser ablation inductively coupled plasma mass spectrometry (LA-ICP-MS) with an Agilent 7500 quadrupole ICP-MS coupled with a resolution SE 193-nm excimer laser at the National Institute of Natural Hazards, Ministryof Emergency Management of China (NINH-MEMC), following the detailed procedures described in Liu et al. (2008). Zircon ^{29}Si concentrations in NIST 610 were used for internal standardization and zircon 91500 was used for external standards. A 30 μm spot size was used in LA-ICP-MS analyses and the common lead correction used the method of Anderson (2002). Concordia ages and diagrams were determined using Isoplot R (Vermeesch, 2018). All calculated ages are quoted with a 1 sigma error.

Zircon and apatite (U-Th)/He dating

Zircon and apatite (U-Th)/He (ZHe and AHe) ages were measured at the NINH-MEMC, Beijing, following standard procedures (Farley and Stockli, 2002; Reiners et al., 2004; Shen et al., 2021, Shen et al. 2022b). After being separated by magnetic and standard heavy liquid mineral separation techniques, >70 μm diameter, euhedral ZHe and AHe grains without visible inclusions, were selected under a microscope for dating. Each grain dimension was measured from digital photographs for an *α* ejection correction, then individual grains were wrapped into a platinum capsule for thermal outgas. Subsequently, He extraction and measurement of ZHe and AHe were conducted by a PrismaPLus QME 220 quadrupole mass spectrometer. Determination of U and Th was carried out on a coupled Agilent 7500 quadrupole ICP-MS. The *α* ejection correction (Farley et al., 1996) was applied to each crystal to calculate and correct the (U-Th)/He ages. We analyzed four single-grain aliquots for ZHe dating and at least two grains for AHe dating for chosen samples.

Thermal history modeling for ZHe and AHe data

To model the thermal evolution of multiple samples, we used the program QTQt (Gallagher, 2012) to simulate the

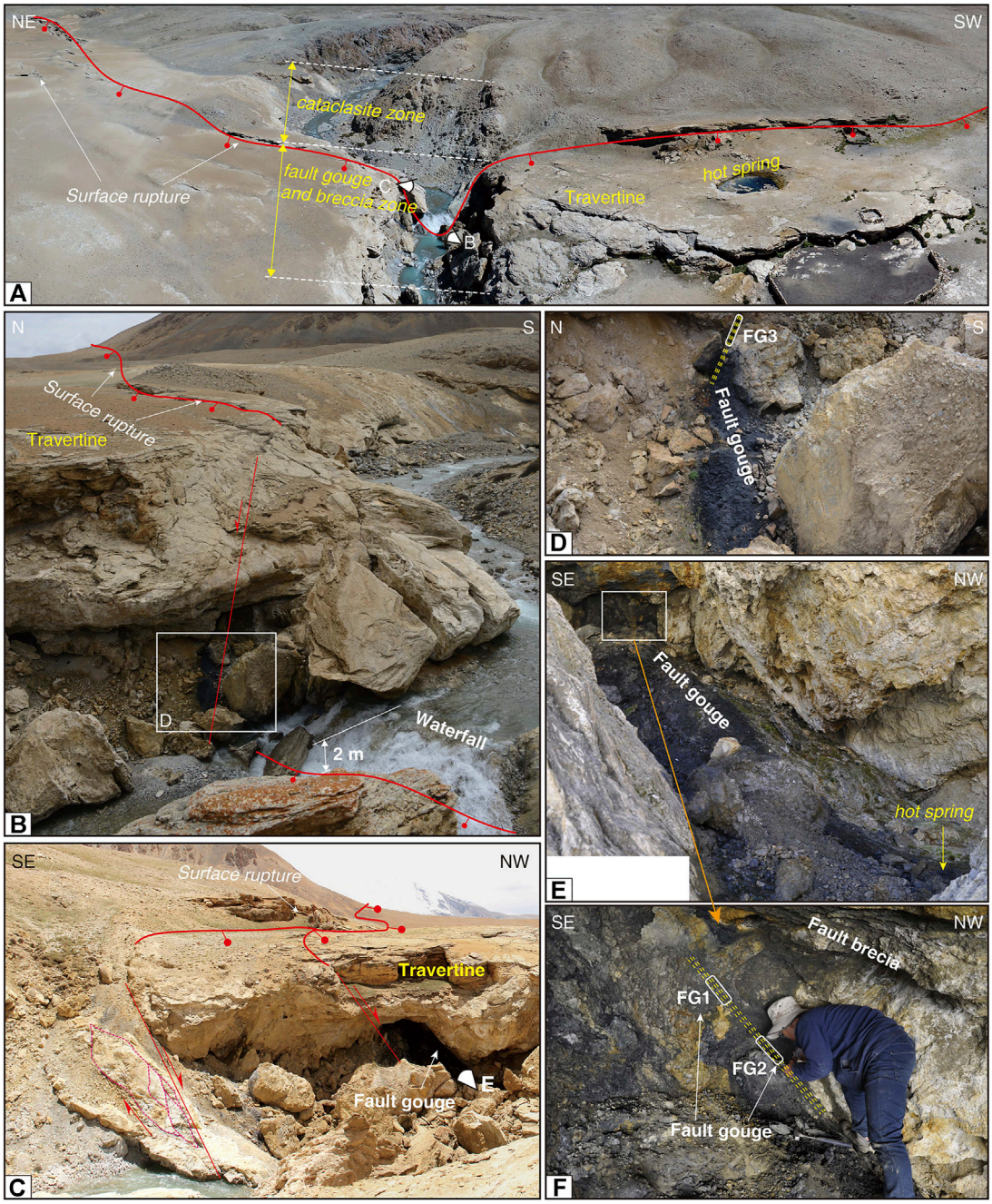

FIGURE 5
Field photos of active normal faults and location of fault gouge samples north of Chumba Yumco lake. **(A)** UAV photo of surface cracks in the travertine and fault rock distribution along active faults. **(B,C)** Exposure of fault gouge beneath the travertine as well as ~2 m-high waterfall due to normal throw. **(D–F)** Black fault gouge where three samples, FG1–FG3, were collected for authigenic illite K-Ar age analyses.

thermal history of footwall leucogranite. In the modeling, He diffusion parameters based on α radiation damage (Flower et al., 2009) and the annealing model of Ketcham et al. (2007) were applied for both ZHe and AHe systems. All samples follow the geological constraints: 1) mean temperature of 10 ± 10 °C for the present-day earth surface; 2) initial time-temperature at ~27 ± 3 Ma (Zircon U-Pb age in our study) and 700 ± 50°C (Zircon U-Pb closure temperature, Copeland et al., 1990); 3) activity time-temperature at 9 ± 1 Ma and 200 ± 50°C of the fault gouge in our study; 4) geothermal gradient is set to ~30°C/km (Clark et al., 2005), and is allowed to vary over time.

TABLE 2 K–Ar ages for the different size fractions of illite isolated from the fault gouge samples.

Sample	Size	K cont.	$(^{40}Ar/^{38}Ar)_m$	$(^{38}Ar/^{36}Ar)_m$	Radiogenic	^{40}K	Age
No.	(μm)	(%)			^{40}Ar (mol/g)	(mol/g)	(Ma, 1σ)
FG1	1–2	5.87	7.94	310.03	6.87×10^{-10}	1.41×10^{-7}	82.2 ± 1.2
	0.25–0.5	5.65	3.70	412.58	4.35×10^{-10}	1.35×10^{-7}	54.4 ± 0.6
	< 0.25	2.24	3.36	298.57	2.20×10^{-10}	5.37×10^{-8}	69.1 ± 0.6
FG2	1–2	3.35	7.33	916.88	7.94×10^{-10}	8.03×10^{-8}	162.6 ± 1.7
	0.5–1	4.52	4.66	791.85	7.84×10^{-10}	1.08×10^{-7}	120.5 ± 1.3
	0.25–0.5	4.7	4.72	361.87	5.90×10^{-10}	1.13×10^{-7}	87.9 ± 0.9
	< 0.25	7.83	5.14	268.01	4.69×10^{-10}	1.88×10^{-7}	42.5 ± 0.6
FG3	1–2	6.15	6.51	404.05	7.15×10^{-10}	1.47×10^{-7}	81.6 ± 0.8
	0.5–1	5.7	4.30	363.84	5.74×10^{-10}	1.37×10^{-7}	70.9 ± 0.6
	0.25–0.5	6.24	3.78	553.42	4.99×10^{-10}	1.50×10^{-7}	56.5 ± 0.7
	< 0.25	5.34	3.12	281.03	2.61×10^{-10}	1.28×10^{-7}	34.8 ± 0.5

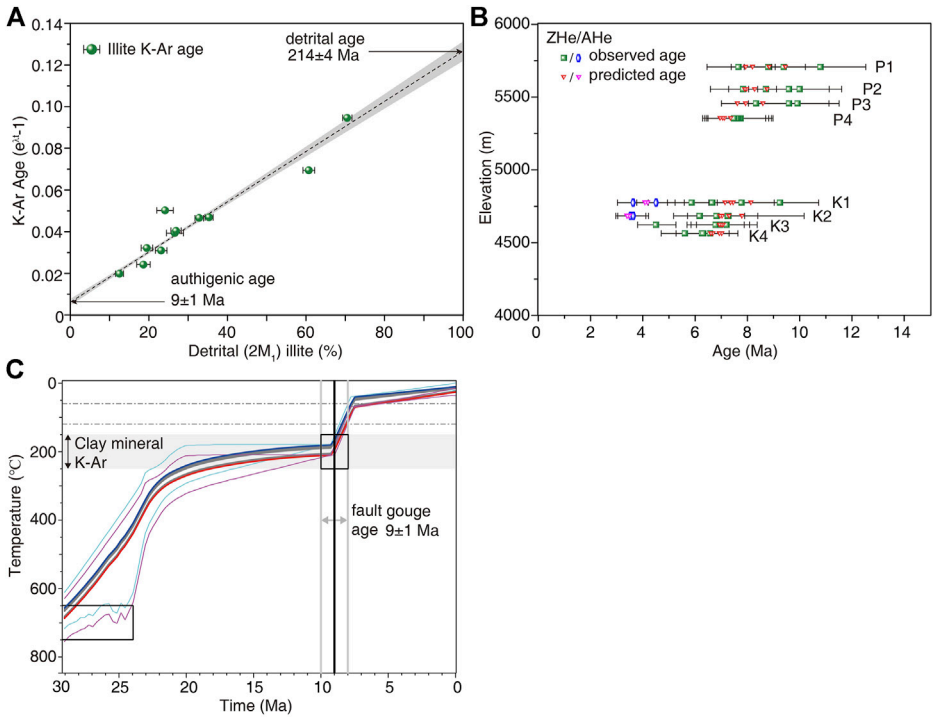

FIGURE 6
Zircon, apatite (U-Th)/He results and fault gouge authigenic illite ages. **(A)** K-Ar ages correlate with the percentage detrital illite component. Authigenic illite ages are late Miocene at 9 ± 1 Ma and detrital illite ages are late Triassic at 214 ± 4 Ma. **(B)** Age-elevation relationship for the northern Chomo Lhari Mountain and southern Chumba Yumco profiles, showing both observed and predicted single-grain ages modeled by QTQt. **(C)** Thermal modeling results of northern Chomo Lhari Mountain and southern Chunba Yumco leucogranite using QTQt Gallagher (2012) with fault gouge dating in the normal Yadong fault. The thick blue, grey, and red lines show the uppermost, intermediate, and lowermost samples, respectively, representing the 95% confidence intervals for the uppermost, intermediate, and lowermost thermal histories. The grey box shows the temperature range of K-Ar dating of Clay mineral in fault gouge Grathoff and Moore (1996).

Results

Fault gouge authigenic illite K-Ar ages

Eleven XRD results and K-Ar ages of different size fractions in three fault gouge samples were obtained. According to the XRD results, no calcite and K-feldspar was visible in the illite of various size fractions (1–2, 0.5–1, 0.25–0.5, and 0.25 μm) (Supplementary Figure S4), with mainly containing $2M_1$ and $1M_d$ polytype illites. Quantification of mineral compositions in the fractions is calculated by the BGMN software. The best-fitting mineral composition curves obtained from BGMN are consistent with the original plot of XRD results (Supplementary Figure S5). The detailed composition and content of illite aliquots are summarized in Supplementary Table S2. In principle, the percentage content of detrital illite ($2M_1$ polytype) decreases with the grain size (Supplementary Table S2).

The K-Ar ages for each illite fraction are listed in Table 2. Aliquot sizes decrease with decreasing $2M_1$ polytype illites, and ages also gradually become younger (Figure 6A). The fine, <0.25 μm fractions in the samples yield ages ranging between 34.8 ± 0.5 and 69.1 ± 0.6 Ma, and the coarse, 1–2 μm fractions yield apparent older ages varying from 81.6 ± 0.8 to 162.6 ± 1.7 Ma. We plot the detrital illite content of different fractions against their K-Ar ages ($e^{\lambda t}$-1) (Figure 6A) with linear fitting used by the York regression (York, 1968) to constrain the end-member ages. We obtain authigenic illite ages of 9 ± 1 Ma at the authigenic end-member, and of 214 ± 4 Ma at the detrital end-member (Figure 6A).

Zircon U–Pb isotopic ages

To determine the crystallization age of the footwall leucogranite, samples P1 and K3 were selected for zircon U–Pb dating. Measurement results are listed in Supplementary Table S3. Zircon grains are euhedral to subhedral in shape, exhibiting clear oscillatory zoning and rim-core domains pattern (Supplementary Figure S1). Both samples show similar characteristics of concordant ages. In sample P1, 119 spots were analyzed. On the concordia plot, the 13 crystal borders of neocrystallisation yielded a late Oligocene $^{206}Pb/^{238}U$ age of 28.80 ± 0.17 Ma. Other spots in crystal cores are concordant and reveal a Cambrian inherited $^{206}Pb/^{238}U$ age of 505.04 ± 0.76 Ma (Supplementary Figures S2A,B). Eighteen zircon grains in sample K1 are concordant and dated at 23.30 ± 0.23 Ma, i.e., late Oligocene-Early Miocene. Other analyzed spots in sample K1 have a Cambrian inheritance $^{206}Pb/^{238}U$ age of 507.79 ± 0.87 Ma (Supplementary Figures S2C,D). Few zircon grains implying a large inheritance from 200 to 500 Ma (Supplementary Figures S2, S3) probably correspond to the mixed value, due to the small grain size or narrow crystal rims.

Zircon and apatite (U-Th)/He ages and thermal modeling results

Four zircon grains were selected in each sample (P1–P4, K1–K4) for ZHe dating. Two apatite grains were collected in each of the samples K1 and K3 for AHe dating. All ZHe cooling ages from the eight samples range from 5.6 to 13.1 Ma, with most ages ranging between ca. 7 and 11 Ma, except one outlier replicate in sample P2 at 25.9 Ma (Table 1), suggesting a possible influence from U-rich neighbouring minerals or U-rich mineral inclusions in the analyzed grain (Shen et al., 2021). All AHe ages in the two samples fall between 8.2 and 9.2 Ma (Figure 6B; Table 1).

Modeling results suggest that the footwall leucogranite may have experienced two stages of rapid cooling since the late Oligocene (Figure 6C). The first stage started at ~28 Ma when the leucogranite formed, as constrained by the zircon U-Pb isotopic ages. During this stage, the leucogranite rapidly cooled at a rate of ~50°C/Myr between ~28 and 20 Ma, after which the leucogranite was in a relatively slow cooling period until ~9 Ma. Then, the second rapid cooling stage started at ~9 Ma and lasted until ~8 Ma with an exhumation rate of ~110°C/Myr, derived from the closure temperature of ZHe (180 ± 20°C, Mahéo et al., 2007) to AHe (70 ± 15°C, Mahéo et al., 2007).

Discussion

Onset timing of the Yadong-Gulu at ~9–8 Ma

Isotopic dating of authigenic illite in faults provides an important approach to directly determining the last primary episode of fault motion in the shallow crust (Zwingmann and Mancktelow, 2004; Van der Pluijm et al., 2006; Duvall et al., 2011; Yamasaki et al., 2013). Previous studies suggest that each well-defined fitting line in the percentage of detrital illite and the K-Ar age usually reveals one single fault event (Duvall et al., 2011; Mottram et al., 2020; Zhao et al., 2022). Linearly extrapolating to the 0% detrital illite of all different size fractions at 9 ± 1 Ma represents the integrated or mean age at which authigenic illite grew (Yamasaki et al., 2013). This average age, 9 ± 1 Ma, also reconciles the rapid exhumation stage determined by ZHe and AHe results (Figure 6C), which most likely indicates the onset timing of normal faulting of the southern YGR (Duvall et al., 2011). Clay minerals K-Ar in fault gouge samples are usually generated in thermal events at 200 ± 50°C (Grathoff and Moore, 1996). Authigenic illite, the $1M_d$ polytype, is thought to reflect the relatively lower temperature of thermal activity at ~200–150°C (Zwingmann and Mancktelow, 2004). Therefore, the formation depth of the YGR fault gouge can be calculated as 9–4 km (using a geothermal gradient of ~23–40°C/km, Francheteau et al., 1984), which is at a similar depth as that of the footwall leucogranite:

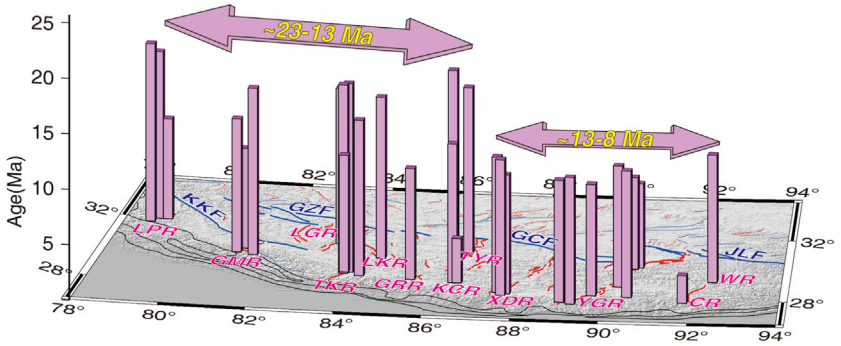

FIGURE 7
Distribution of onset timing for the main ~NS-trending rifts in southern Tibet. The majority of ages shows old initiation timing from ~23 to 13 Ma west of Xainza-Dinggye rift (XDR) and young onset timing from ~13 to 8 Ma east of XDR. CR, Cona rift; GMR, Gurla Mandhata rift; GRR, Gyirong rift; KCR, Kung Co rift; LGR, Lunggar rift; LPR, Leo Pargil rift; TKR, Thakkhola rift; WR, Woka rift; XDR, Xainza-Dinggye rift; YGR, Yadong-Gulu rift. GCF, Gyaring Co fault; GZF, Gaize fault; JLF, Jiali fault; KKF, Karakorum fault.

7.8–4.5 km at ~9 Ma. Contemporaneous rapid exhumation of the footwall leucogranite and the mean age of authigenic illite of fault with their consistent depth at ~9 Ma provides clear evidence that rapid exhumation directly results from the activity of the boundary normal fault of the southern YGR.

Near the Khula Kangri Mountain (Figure 2A), located ~90 km east of Chumba Yumco lake, Edwards and Harrison (1997) suggested that the detachment motion of the STDS continued to 12.5 ± 0.4 Ma, the date when monazite crystalized in the leucogranite. Therefore, these authors further inferred that the Yadong normal fault formed after the youngest crystallization age (~10 Ma), cutting across the STDS. By measuring U-Pb dating of granite cut by the normal fault bounding the eastern part of the southernmost YGR, Ratschbacher et al. (2011) obtained a maximum onset timing of 11.5 ± 0.4 Ma. Both results suggest an upper onset timing limit of the southernmost YGR. Thus, the authigenic illite with 9 ± 1 Ma K-Ar age probably derives from the hydrothermal effect created by the initiation timing of the YGR, following a rapid and strong activity of the boundary fault. Considering the initiation age of 8 ± 1 Ma in the northern YGR along the Nyainqentanglha mountain (Figure 1B; Harrison et al., 1995; Kapp et al., 2005), we propose that E-W extension along the different sections of the YGR occurred contemporaneously at ~9–8 Ma.

Recently, Bian et al. (2022) proposed that the southern Yadong-Gulu rift initiated at ~13–11 Ma in the south, using (U-Th)/He and fission track low-temperature thermochronology, and later northwards, at ~8 Ma (Harrison et al., 1995). They argued that such spatial and temporal pattern was influenced by the outward expansion of the Himalayan arc. However, since most of their samples are located quite far, ~20 km for some samples, from the main active Yadong normal fault of the southern YGR, and closer to the active thrusts along the Himalaya (such as the Main Boundary Thrust, MBT), their uplift may instead be influenced more by the MBT or regional uplift of Himalayan orogenic belt. Our fault gouge and leucogranite samples were taken in or near the fault plane, therefore, we argue that our new illite K-Ar age in fault gouge and (U-Th)/He dating of footwall leucogranite provide direct evidence of the fault activity and represent the onset timing of the YGR. Thus, the 9 ± 1 Ma onset timing in the southern YGR (this study) and 8 ± 1 Ma (Harrison et al., 1995) in the northern YGR, suggest that E-W extension along the YGR occurred contemporaneously along its ~500 km length from south to north.

Cooling history of the Yadong-Gulu footwall leucogranite

Although the two elevation transects, P1–P4 and K1–K4, are located in different leucogranite bodies, the two transect samples yielded similar zircon U-Pb ages (Supplementary Figures S2, S3). Thus, samples P1–P4 and K1–K4 probably experienced a uniform cooling history in the Pagri graben. For samples P1 and K3, both zircon U-Pb dating show similar rim ages ranging between 28.8 ± 0.17 and 23.3 ± 0.23 Ma. These two late Oligocene ages suggest that the leucogranite crystallization formed due to the motion of the STDS, which primarily occurred at ~23 Ma and ended before ~13 Ma (e.g., Edwards and Harrison, 1997; Grujic et al., 2002; Leloup et al., 2010; Cooper et al., 2015). Combined with the ~22–14 Ma biotite ^{40}Ar-^{39}Ar ages in the leucogranite north of Chomo Lhari mountain (Regional, 2004), we constrain the first rapid cooling of the footwall leucogranite at ~50 ± 20°C/Myr from the 700 ± 50°C zircon U-Pb closure temperature (Copeland et al., 1990) to 300 ± 30°C for Ar in biotite (Mahéo et al., 2007).

The age-elevation section and the modeling results of ZHe and AHe imply that the second rapid cooling of the

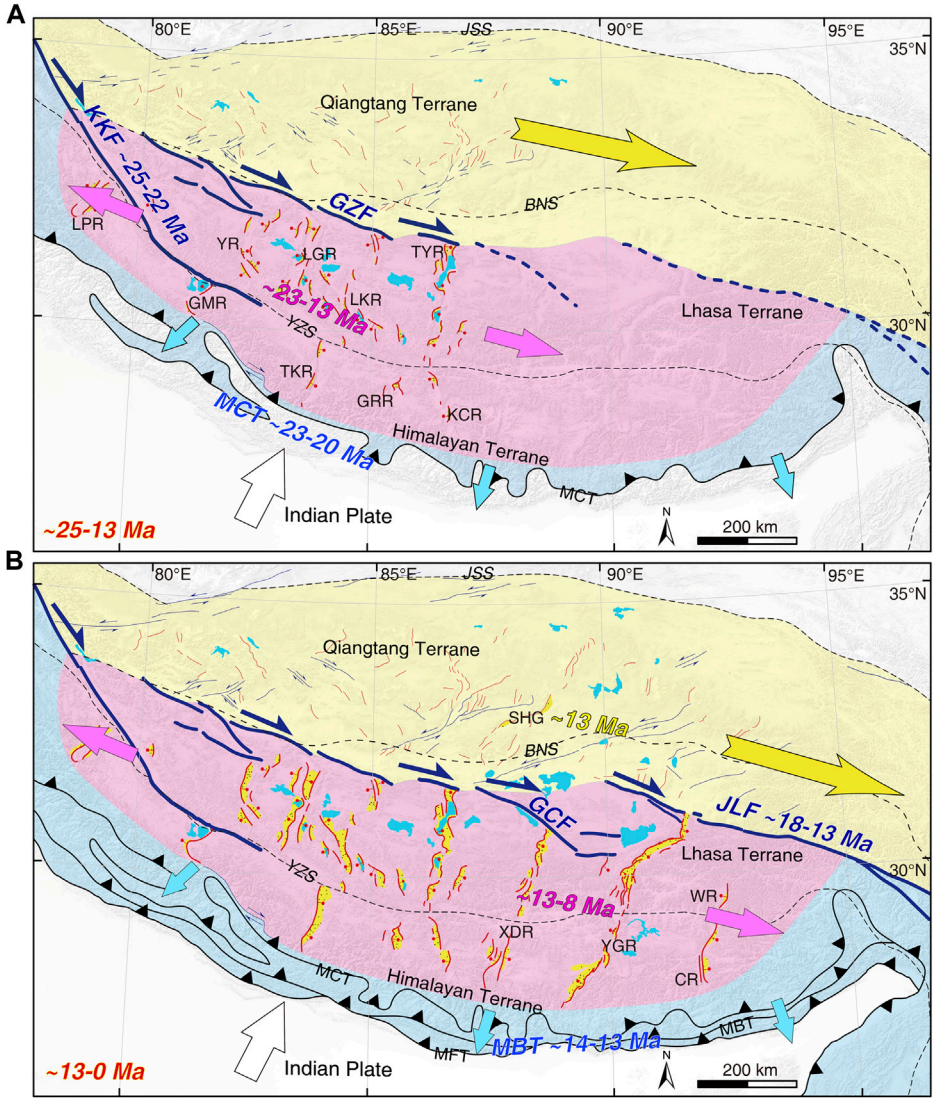

FIGURE 8
E-W extension kinematic model of southern Tibet. **(A)** Formation of rifts in the western half of southern Tibet are controlled by the Karakorum-Gaize fault (~25–22 Ma) and Main Central Tibet (~23–20 Ma). **(B)** Rifts in the eastern half of southern Tibet formed by eastward propagation of Gyaring Co-Jiali fault (~18–13 Ma) and Main Boundary fault (~14–13 Ma) along the curved Himalayan arc. Age references are listed in Supplementary Tables S1, S4. Yellow area and arrow represent the eastward extrusion of Qiangtang terrane. Pink area and arrows represent the E-W extension of arcuate southern Tibet. Blue area and arrows represent the divergent orthogonal thrusting along the curved Himalayan arc. Main rifts and sutures are: CR, Cona rift; GMR, Gurla Mandhata rift; GRR, Gyirong rift; KCR, Kung Co rift; LGR, Lunggar rift; LPR, Leo Pargil rift; SHG, Shuanghu graben; TKR, Thakkhola rift; TYR, Tangra Yumco rift; WR, Woka rift; XDR, Xainza-Dinggye rift; YGR, Yadong-Gulu rift; YR, Yari rift; GCF, Gyaring Co fault; GZF, Gaize fault; JLF, Jiali fault; KKF, Karakorum fault; MBT, Main boundary fault; MCT, Main central fault; MFT, Main frontal thrust; NQTL, Nyainqentanglha; BNS, Bangong-Nujiang suture; JSS, Jinsha suture; YZS, Yarlung Zangbo suture.

leucogranite especially occurred around ~9–8 Ma (Figures 6B,C). ZHe mean ages of samples K1 and K3 are 8.8 ± 1.5 and 8.6 ± 1.1 Ma, respectively, and AHe ages are 8.7 ± 0.4 and 8.5 ± 0.2 Ma (Figure 6B; Table 1). In the modeling results (Figure 6C), the leucogranite had a rapid exhumation from ~9 Ma to ~8 Ma. Given the ~23–40°C/km geothermal gradient in southern Tibet (Francheteau et al., 1984) and the closure temperature of ZHe (180 ± 20°C, Mahéo et al., 2007) and AHe (70 ± 15°C, Mahéo et al., 2007), we can calculate a minimum exhumation rate of ~3.5 ± 1 mm/yr in this narrow timescale (~9–8 Ma) from depths of 7.8–4.5 to 3.0–1.7 km. After ~8 Ma, the leucogranite started its slow exhumation near the Earth's surface at a rate of 0.4–0.2 mm/yr.

Implications for E-W extension in the southern Tibetan Plateau

In recent decades, several detailed geochronology studies have been conducted for the E-W extension in southern Tibet, using zircon or monazite U-Th/Pb, mica $^{40}Ar/^{39}Ar$, and low-temperature thermochronology [fission track, (U-Th)/He] methods (Supplementary Table S1). At least seven main, ~NS-trending rifts resulting from E-W extension are located in southern Tibet (e.g., Armijo et al., 1986). West of the Xainza-Dinggye rift (XDR), the oldest, published onset timing for each of the main rifts, such as the Leo Pargil, Yari, Gurla Mandhata, Lunggar, Thakkhola, Gyirong, Tangra Yumco, and Kung Co rifts, were constrained at ~23–15 Ma by zircon U-Pb, apatite and zircon (U-Th)/He, as well as fission track dating (Figure 1C; e.g., Langille et al., 2012; Mitsuishi et al., 2012; Styron et al., 2013; McCallister et al., 2014; Shen et al., 2016; Wolff et al., 2019; Brubacher et al., 2021; Larson et al., 2020). By contrast, east of the XDR, the YGR, Cona, and Woka rifts show relatively young initiation timing at <13 Ma, and as recent as 2 Ma (Figure 1C; Supplementary Table S1; Harrison et al., 1995; Kapp et al., 2005; Cottle et al., 2009; Kali et al., 2010; Leloup et al., 2010; Bian et al., 2020, 2022; Shen et al., 2022a). Overall, initiation ages indicate an old to the west and young to the east of the XDR accomodating E-W extension in southern Tibet (Figure 7).

Such eastward younging of the south Tibetan rifts, and synchronous onset timing of the entire YGR have important implications for understanding and re-evaluating the proposed tectonic models of E-W extension in southern Tibet. Orogenic collapse model (Dewey, 1988) has been proposed as a mechanism for E-W extension, in which the collapse mainly occurs eastward, and extension should be predominant to the east (e.g., Copley, 2008). Delamination of thickened mantle lithosphere (England and Houseman, 1989), predicts that E-W extension occurred simultaneously in all rifts southern Tibet. Both models are inconsistent with the eastward younging pattern we suggest here. On the other hand, dynamics from the tearing of subducting Indian lithospheric slab (e.g., Replumaz et al., 2010; Chen et al., 2015), yields ages to decrease eastwards, but more related to a eastward wave of uplift, than a wave of extension. Thus, lithospheric dynamic models are inappropriate in dealing with the observed deformation.

Given the absence of mechanical coupling between the underthrusting Indian lithosphere beneath southern Tibet and upper crustal deformation (Wang et al., 2022), the main dynamics driving the initiation of E-W extension should instead be related to the boundary forces, in link with the Karakorum-Jiali fault zone (KJFZ) accommodating eastward extrusion of central/northern Tibet, as well as the thrusting along the Himalayan arc. In this model, the development of the south Tibetan rifts may be divided in two stages (Figures 8A,B, Supplementary Table S4, and references therein): the first stage at ~23–13 Ma, during which rifting in the arcuate western half of the southern Tibet bounded by the Main Central Thrust (active since ~23–20 Ma) was triggered by the right-lateral strike slip of Karakorum-Gaize faults (active since ~25–22 Ma, Figure 8A; Supplementary Table S4); the second stage started at ~13 Ma, during which rifting in the eastern half of the southern Tibet bounded by the Main Boundary Thrust (active since ~14–13 Ma) was triggered by the right-lateral strike slip of Gyaring Co-Jiali faults (active since ~18–13 Ma, Figure 8B; Supplementary Table S4). Such E-W extension accommodates the ongoing orthogonal and divergent thrusting along the curved Himalayan arc (Armijo et al., 1986, 1989).

Conclusion

Our new authigenic illite K-Ar age and (U-Th)/He thermochronology confirm the onset timing of southern Yadong-Gulu rift at 9 ± 1 Ma. Combined with previous data from the northern YGR, our results suggest contemporary formation of the entire YGR at ~9–8 Ma. Overall, the onset timing of the seven ~NS-trending south Tibetan rifts appear to formed earlier to the west from ~23–13 Ma and later to the east from ~13 Ma. Therefore, we suggest that E-W extension in southern Tibet was driven by a combination of eastward propagation along the Karakorum-Jiali fault zone, together with divergent thrusting along the curved Himalayan arc.

Data availability statement

The original contributions presented in the study are included in the article/Supplementary Material, further inquiries can be directed to the corresponding author.

Author contributions

SW did the field work, interpreted the data and wrote the paper. XS interpreted the data and contributed to the modeling. M-LC and AR discussed, interpreted the data, and improved the manuscript including figures. YZ and JP did the field work. YZ, HL, JP, KL and XX discussed and improved the figures.

Funding

This research was financially supported by the second Tibetan Plateau Scientific Expedition and Research Program (STEP) (2019QZKK0708), Scientific Research Fund of the National Institute of Natural Hazards, MEMC (ZDJ2019-19), the Ministry of Science and Technology of China (2019QZKK0901, 2021FY100101), the Key Special Project for Introduced Talents Team of the Southern Marine Science and Engineering Guangdong Laboratory (GML2019ZD0201), the China Geological Survey (DD20221630), and Institute of Geology, Chinese Academy of Geological Sciences (J1901-30, J2201).

Acknowledgments

We thank Mingkun Bai and Fucai Liu for their help in the field. We thank the Lab at NINH-MEMC for analyzing the samples and Haijia Lei for experiment. Constructive reviews by the reviewers as well as editorial work are gratefully appreciated.

Conflict of interest

The authors declare that the research was conducted in the absence of any commercial or financial relationships that could be construed as a potential conflict of interest.

Publisher's note

All claims expressed in this article are solely those of the authors and do not necessarily represent those of their affiliated organizations, or those of the publisher, the editors and the reviewers. Any product that may be evaluated in this article, or claim that may be made by its manufacturer, is not guaranteed or endorsed by the publisher.

Supplementary material

The Supplementary Material for this article can be found online at: https://www.frontiersin.org/articles/10.3389/feart.2022.993796/full#supplementary-material

References

Anderson, T. (2002). Correction of common lead in U–Pb analyses that do not report ^{204}Pb. *Chem. Geol.* 192, 59–79. doi:10.1016/S0009-2541(02)00195-X

Armijo, R., Tapponnier, P., and Han, T. L. (1989). Late Cenozoic right-lateral strike-slip faulting in southern Tibet. *J. Geophys. Res.* 94 (B3), 2787–2838. doi:10.1029/JB094iB03p02787

Armijo, R., Tapponnier, P., Mercier, J. L., and Han, T. L. (1986). Quaternary extension in southern Tibet: Field observations and tectonic implications. *J. Geophys. Res.* 91 (14), 13803–13872. doi:10.1029/JB091iB14p13803

Bergmann, J., Friedel, P., and Kleeberg, R. (1998). BGMN-a new fundamental parameter based Rietveld program for laboratory X-ray sources, its use in quantitative analysis and structure investigations. *Comm. Powder Diffr. Newsl.* 20, 5–8. doi:10.1346/CCMN.1998.0460209

Bian, S., Gong, J., Zuza, A. V., Yang, R., Chen, L., Ji, J., et al. (2022). Along-strike variation in the initiation timing of the north-trending rifts in southern Tibet as revealed from the Yadong-Gulu rift. *Tectonics* 41, e2021TC007091. doi:10.1029/2021TC007091

Bian, S., Gong, J., Zuza, A. V., Yang, R., Tian, Y., Ji, J., et al. (2020). Late Pliocene onset of the Cona rift, eastern Himalaya, confirms eastward propagation of extension in Himalayan-Tibetan orogen. *Earth Planet. Sci. Lett.* 544, 116383. doi:10.1016/j.epsl.2020.116383

Brubacher, A. D., Larson, K. P., Cottle, J. M., Matthews, W., and Camacho, A. (2021). Progressive development of EW extension across the Tibetan plateau: A case study of the Thakkhola graben, west-central Nepal. *Int. Geol. Rev.* 63 (15), 1900–1919. doi:10.1080/00206814.2020.1808860

Chen, Y., Li, W., Yuan, X., Badal, J., and Teng, J. (2015). Tearing of the Indian lithospheric slab beneath southern Tibet revealed by SKS-wave splitting measurements. *Earth Planet. Sci. Lett.* 413, 13–24. doi:10.1016/j.epsl.2014.12.041

Chevalier, M. L., Replumaz, A., Wang, S., Pan, J., Bai, M., Li, K., et al. (2022). Limit of monsoonal precipitation in southern Tibet during the Last Glacial Maximum from relative moraine extents. *Geomorphology* 397, 108012. doi:10.1016/j.geomorph.2021.108012

Chevalier, M. L., Tapponnier, P., van der Woerd, J., Leloup, P. H., Wang, S., Pan, J., et al. (2020). Late Quaternary extension rates across the northern half of the Yadong-Gulu rift: Implication for east-west extension in southern Tibet. *J. Geophys. Res. Solid Earth* 125 (7), e2019JB019106. doi:10.1029/2019JB019106

Clark, M. K., House, M. A., Royden, L. H., Whipple, K. X., Burchfiel, B. C., Zhang, X., et al. (2005). Late cenozoic uplift of southeastern Tibet. *Geol.* 33 (6), 525–528. doi:10.1130/G21265.1

Coleman, M., and Hodges, K. (1995). Evidence for Tibetan plateau uplift before 14 Myr ago from a new minimum age for east–west extension. *Nature* 374 (6517), 49–52. doi:10.1038/374049a0

Cooper, F. J., Hodges, K. V., Parrish, R. R., Roberts, N. M. W., and Horstwood, M. S. A. (2015). Synchronous N-S and E-W extension at the Tibet-to-Himalaya transition in NW Bhutan. *Tectonics* 34 (7), 1375–1395. doi:10.1002/2014TC003712

Copeland, P., Harrison, T. M., and Fort, P. L. (1990). Age and cooling history of the manaslu granite: Implications for himalayan tectonics. *J. Volcanol. Geotherm. Res.* 44 (1-2), 33–50. doi:10.1016/0377-0273(90)90010-D

Copley, A. (2008). Kinematics and dynamics of the southeastern margin of the Tibetan Plateau. *Geophys. J. Int.* 174 (3), 1081–1100. doi:10.1111/j.1365-246X.2008.03853.x

Cottle, J. M., Jessup, M. J., Newell, D. L., Horstwood, M. S. A., Noble, S. R., Parrish, R. R., et al. (2009). Geochronology of granulitized eclogite from the ama drime massif: Implications for the tectonic evolution of the South Tibetan Himalaya. *Tectonics* 28 (1), TC1002. doi:10.1029/2008TC002256

DeCelles, P. G., Robinson, D. M., and Zandt, G. (2002). Implications of shortening in the Himalayan fold-thrust belt for uplift of the Tibetan Plateau. *Tectonics* 21 (6), 12–25. doi:10.1029/2001TC001322

Dewey, J. F. (1988). Extensional collapse of orogens. *Tectonics* 7 (6), 1123–1139. doi:10.1029/TC007i006p01123

Dong, H., Larson, K. P., Kellett, D. A., Xu, Z., Li, G., Cao, H., et al. (2021). Timing of slip across the south Tibetan detachment system and yadong–gulu graben, eastern Himalaya. *J. Geol. Soc. Lond.* 178 (1). doi:10.1144/jgs2019-197

Duvall, A. R., Clark, M. K., van der Pluijm, B. A., and Li, C. (2011). Direct dating of Eocene reverse faulting in northeastern Tibet using Ar-dating of fault clays and low-temperature thermochronometry. *Earth Planet. Sci. Lett.* 304 (3-4), 520–526. doi:10.1016/j.epsl.2011.02.028

Edwards, M. A., and Harrison, T. M. (1997). When did the roof collapse? Late Miocene north-south extension in the high Himalaya revealed by Th–Pb monazite dating of the Khula Kangri granite. *Geology* 25, 543–546. doi:10.1130/0091-7613(1997)025<0543:WDTRCL>2.3.CO;2

England, P., and Houseman, G. (1989). Extension during continental convergence, with application to the Tibetan Plateau. *J. Geophys. Res.* 94 (12), 17561–17579. doi:10.1029/JB094iB12p17561

Farley, K. A., and Stockli, D. F. (2002). U-Th)/He dating of phosphates: Apatite, monazite, and xenotime. *Rev. Mineralogy Geochem.* 48, 559–577. doi:10.2138/rmg.2002.48.15

Farley, K. A., Wolf, R. A., and Silver, L. T. (1996). The effects of long alpha-stopping distances on (U-Th)/He ages. *Geochimica Cosmochimica Acta* 60, 4223–4229. doi:10.1016/s0016-7037(96)00193-7

Flowers, R. M., Ketcham, R. A., Shuster, D. L., and Farley, K. A. (2009). Apatite (U-Th)/He thermochronometry using a radiation damage accumulation and annealing model. *Geochimica Cosmochimica Acta* 73, 2347–2365. doi:10.1016/j.gca.2009.01.015

Francheteau, J., Jaupart, C., Shen, X., Kang, W., Lee, D., Bai, J., et al. (1984). High heat flow in southern Tibet. *Nature* 307 (5946), 32–36. doi:10.1038/307032a0

Gallagher, K. (2012). Transdimensional inverse thermal history modeling for quantitative thermochronology. *J. Geophys. Res.* 117, B02408. doi:10.1029/2011jb008825

Grathoff, G. H., and Moore, D. M. (1996). Illite polytype quantification using WILDFIRE© calculated X-ray diffraction patterns. *Clays clay Minerals* 44 (6), 835–842. doi:10.1346/CCMN.1996.0440615

Grujic, D., Hollister, L. S., and Parrish, R. R. (2002). Himalayan metamorphic sequence as an orogenic channel: Insight from Bhutan. *Earth Planet. Sci. Lett.* 198 (1-2), 177–191. doi:10.1016/S0012-821X(02)00482-X

Haines, S. H., and van der Pluijm, B. A. (2010). Dating the detachment fault system of the ruby mountains, Nevada: Significance for the kinematics of low-angle normal faults. *Tectonics* 29, TC4028. doi:10.1029/2009TC002552

Harrison, T. M., Copeland, P., Kidd, W. S. F., and Lovera, O. M. (1995). Activation of the Nyainqentanghla shear zone: Implications for uplift of the southern Tibetan Plateau. *Tectonics* 14 (3), 658–676. doi:10.1029/95TC00608

Kali, E., Leloup, P. H., Arnaud, N., Maheo, G., Liu, D. Y., Boutonnet, E., et al. (2010). Exhumation history of the deepest central Himalayan rocks Ama Drime range: Key pressure-temperature-deformation-time constraints on orogenic models. *Tectonics* 29, TC2014. doi:10.1029/2009TC002551

Kapp, J. L. D., Harrison, T. M., Kapp, P., Grove, M., Lovera, O. M., and Ding, L. (2005). Nyainqentanglha Shan: A window into the tectonic, thermal, and geochemical evolution of the Lhasa block, southern Tibet. *J. Geophys. Res.* 110, B08413–B08669. doi:10.1029/2004JB003330

Ketcham, R. A., Carter, A., Donelick, R. A., Barbarand, J., and Hurford, A. J. (2007). Improved modeling of fission-track annealing in apatite. *Am. Mineralogist* 92, 799–810. doi:10.2138/am.2007.2281

Klootwijk, C. T., Conaghan, P. J., and Powell, C. M. (1985). The Himalayan arc: Large-scale continental subduction, oroclinal bending and back-arc spreading. *Earth Planet. Sci. Lett.* 75 (2-3), 167–183. doi:10.1016/0012-821X(85)90099-8

Langille, J. M., Jessup, M. J., Cottle, J. M., Lederer, G., and Ahmad, T. (2012). Timing of metamorphism, melting and exhumation of the Leo Pargil dome, northwest India. *J. Metamorph. Geol.* 30 (8), 769–791. doi:10.1111/j.1525-1314.2012.00998.x

Larson, K. P., Kellett, D. A., Cottle, J. M., Camacho, A., and Brubacher, A. D. (2020). Mid-Miocene initiation of E-W extension and recoupling of the Himalaya. *Terra Nova* 32 (2), 151–158. doi:10.1111/ter.12443

Leloup, P. H., Mahéo, G., Arnaud, N., Kali, E., Boutonnet, E., Liu, D., et al. (2010). The South Tibet detachment shear zone in the Dinggye area: Time constraints on extrusion models of the Himalayas. *Earth Planet. Sci. Lett.* 292 (1-2), 1–16. doi:10.1016/j.epsl.2009.12.035

Liu, Y., Hu, Z., Gao, S., Günther, D., Xu, J., Gao, C., et al. (2008). *In situ* analysis of major and trace elements of anhydrous minerals by LA-ICP-MS without applying an internal standard. *Chem. Geol.* 257, 34–43. doi:10.1016/j.chemgeo.2008.08.004

Mahéo, G., Leloup, P. H., Valli, F., Lacassin, R., Arnaud, N., Paquette, J. L., et al. (2007). Post 4 ma initiation of normal faulting in southern Tibet. constraints from the Kung Co half graben. *Earth Planet. Sci. Lett.* 256 (1-2), 233–243. doi:10.1016/j.epsl.2007.01.029

McCaffrey, R., and Nabelek, J. (1998). Role of oblique convergence in the active deformation of the Himalayas and southern Tibet plateau. *Geol.* 26, 691–694. doi:10.1130/00917613(1998)026<0691:ROOCIT>2.3.CO;2

McCallister, A. T., Taylor, M. H., Murphy, M. A., Styron, R. H., and Stockli, D. F. (2014). Thermochronologic constraints on the late Cenozoic exhumation history of the Gurla Mandhata metamorphic core complex, Southwestern Tibet. *Tectonics* 33, 27–52. doi:10.1002/2013TC003302

Meesters, A. G. C. A., and Dunai, T. J. (2002). Solving the production-diffusion equation for finite diffusion domains of various shapes. *Chem. Geol.* 186, 347–364. doi:10.1016/s0009-2541(02)00073-6

Mitsuishi, M., Wallis, S. R., Aoya, M., Lee, J., and Wang, Y. (2012). E–W extension at 19 Ma in the Kung Co area, S. Tibet: Evidence for contemporaneous E–W and N–S extension in the Himalayan orogen. *Earth Planet. Sci. Lett.* 325, 10–20. doi:10.1016/j.epsl.2011.11.013

Mottram, C. M., Kellett, D. A., Barresi, T., Zwingmann, H., Friend, M., Todd, A., et al. (2020). Syncing fault rock clocks: Direct comparison of U-Pb carbonate and K-Ar illite fault dating methods. *Geology* 48 (12), 1179–1183. doi:10.1130/G47778.1

Peng, X., Chen, Y., Liu, B., Liu, G., Liu, Q., and Liu, J. (2018). Timing and features of a late MIS 2 rock avalanche in the Eastern Himalayas, constrained by ^{10}Be exposure dating. *Geomorphology* 318, 58–68. doi:10.1016/j.geomorph.2018.05.022

Ratschbacher, L., Krumrei, I., Blumenwitz, M., Staiger, M., Gloaguen, R., Miller, B. V., et al. (2011). Rifting and strike-slip shear in central Tibet and the geometry, age and kinematics of upper crustal extension in Tibet. *Geol. Soc. Lond. Spec. Publ.* 353 (1), 127–163. doi:10.1144/SP353.8

Regional (2004). *1: 250000 regional geological maps (G45C001004, H45C004004)*. Beijing: China University of Geosciences. (in Chinese).

Reiners, P. W., Spell, T. L., Zanetti, N. S., and Zanetti, K. A. (2004). Zircon (U-Th)/He thermochronometry: He diffusion and comparisons with ^{40}Ar/^{39}Ar dating. *Geochim. Cosmochim. Acta* 68 (8), 1857–1887. doi:10.1016/j.gca.2003.10.021

Replumaz, A., Negredo, M., Villasenor, N., and Guillot, S. (2010). Indian continental subduction and slab break-off during Tertiary Collision. *Terra Nova* 22 (4), 290–296. doi:10.1111/j.1365-3121.2010.00945.x

Royden, L. H., Burchfiel, B. C., King, R. W., Wang, E., Chen, Z., Shen, F., et al. (1997). Surface deformation and lower crustal flow in eastern Tibet. *Science* 276 (5313), 788–790. doi:10.1126/science.276.5313.788

Shen, T., Wang, G., Leloup, P. H., van der Beek, P., Bernet, M., Cao, K., et al. (2016). Controls on Cenozoic exhumation of the Tethyan Himalaya from fission-track thermochronology and detrital zircon U-Pb geochronology in the Gyirong basin area, southern Tibet. *Tectonics* 35 (7), 1713–1734. doi:10.1002/2016TC004149

Shen, T., Wang, G., van der Beek, P., Bernet, M., Chen, Y., Zhang, P., et al. (2022a). Impacts of late Miocene normal faulting on Yarlung tsangpo river evolution, southeastern Tibet. *Geol. Soc. Am. Bull.* doi:10.1130/B36210.1

Shen, X., Tian, Y., Wang, Y., Wu, L., Jia, Y., Tang, X., et al. (2021). Enhanced quaternary exhumation in the central three rivers region, southeastern Tibet. *Front. Earth Sci. (Lausanne).* 9, 741491. doi:10.3389/feart.2021.741491

Shen, X., Braun, J., and Yuan, X. (2022b). Southeastern margin of the Tibetan Plateau stopped expanding in the late Miocene. *Earth Planet. Sci. Lett.* 583, 117446. doi:10.1016/j.epsl.2022.117446

Steiger, R. H., and Jäger, E. (1977). Subcommission on geochronology: Convention on the use of decay constants in geo-and cosmochronology. *Earth Planet. Sci. Lett.* 36 (3), 359–362. doi:10.1016/0012-821X(77)90060-7

Styron, R. H., Taylor, M. H., Sundell, K. E., Stockli, D. F., Oalmann, J. A., Moeller, A., et al. (2013). Miocene initiation and acceleration of extension in the South Lunggar rift, Western Tibet: Evolution of an active detachment system from structural mapping and (U-Th)/He thermochronology. *Tectonics* 32 (4), 880–907. doi:10.1002/tect.20053

Sundell, K. E., Taylor, M. H., Styron, R. H., Stockli, D. F., Kapp, P., Hager, C., et al. (2013). Evidence for constriction and Pliocene acceleration of east-west extension in the North Lunggar rift region of west central Tibet. *Tectonics* 32 (5), 1454–1479. doi:10.1002/tect.20086

Tapponnier, P., Mercier, J. L., Armijo, R., Tonglin, H., and Ji, Z. (1981). Field evidence for active normal faulting in Tibet. *Nature* 294 (5840), 410–414. doi:10.1038/294410a0

Tapponnier, P., Peltzer, G., Dain, A., Armijo, R., and Cobbold, P. (1982). Propagating extrusion tectonics in asia: New insights from simple experiments with plasticine. *Geol.* 10 (12), 611. doi:10.1130/0091-7613(1982)10<611:PETIAN>2.0.CO;2

Tapponnier, P., Xu, Z. Q., Roger, F., Meyer, B., Arnaud, N., Wittlinger, G., et al. (2001). Oblique stepwise rise and growth of the Tibet plateau. *Science* 294 (5547), 1671–1677. doi:10.1126/science.105978

Ufer, K., Kleeberg, R., Bergmann, J., and Dohrmann, R. (2012). Rietveld refinement of disordered illite–smectite mixed-layer structures by a recursive algorithm. II: Powder-pattern refinement and quantitative phase analysis. *Clays Clay Min.* 60 (5), 535–552. doi:10.1346/CCMN.2012.0600508

Van der Pluijm, B. A., Hall, C. M., Vrolijk, P. J., Pevear, D. R., and Covey, M. C. (2001). The dating of shallow faults in the Earth's crust. *Nature* 412 (6843), 172–175. doi:10.1038/35084053

Van der Pluijm, B. A., Vrolijk, P. J., Pevear, D. R., Hall, C. M., and Solum, J. (2006). Fault dating in the Canadian rocky mountains: Evidence for late cretaceous and early eocene orogenic pulses. *Geol.* 34 (10), 837–840. doi:10.1130/G22610.1

Velde, B. (1965). Phengite micas; synthesis, stability, and natural occurrence. *Am. J. Sci.* 263 (10), 886–913. doi:10.2475/ajs.263.10.886

Vermeesch, P. (2018). Isoplot R: A free and open toolbox for geochronology. *Geosci. Front.* 9 (5), 1479–1493. doi:10.1016/j.gsf.2018.04.001

Wang, S., Chevalier, M. L., Pan, J., Bai, M., Li, K., Li, H., et al. (2020). Quantification of the late Quaternary throw rates along the Yadong rift, southern Tibet. *Tectonophysics* 790, 228545. doi:10.1016/j.tecto.2020.228545

Wang, S., Replumaz, A., Chevalier, M. L., and Li, H. (2022). Decoupling between upper crustal deformation of southern Tibet and underthrusting of Indian lithosphere. *Terra nova.* 34 (1), 62–71. doi:10.1111/ter.12563

Wolff, R., Hetzel, R., Dunkl, I., Xu, Q., Bröcker, M., and Anczkiewicz, A. A. (2019). High-angle normal faulting at the Tangra Yumco graben (southern Tibet) since- 15 ma. *J. Geol.* 127 (1), 15–36. doi:10.1086/700406

Wu, C., Nelson, K. D., Wortman, G., Samson, S. D., Yue, Y., Li, J., et al. (1998). Yadong cross structure and South Tibetan Detachment in the East Central Himalaya (89–90 E). *Tectonics* 17 (1), 28–45. doi:10.1029/97TC03386

Wu, Z., Ye, P., Barosh, P., and Wu, Z. (2011). The October 6, 2008 Mw 6.3 magnitude Damxung earthquake, Yadong-Gulu rift, Tibet, and implications

for present-day crustal deformation within Tibet. *J. Asian Earth Sci.* 40 (4), 943–957. doi:10.1016/j.jseaes.2010.05.003

Yamasaki, S., Zwingmann, H., Yamada, K., Tagami, T., and Umeda, K. (2013). Constraining the timing of brittle deformation and faulting in the Toki granite, central Japan. *Chem. Geol.* 351, 168–174. doi:10.1016/j.chemgeo.2013.05.005

Yin, A., and Taylor, M. H. (2011). Mechanics of V-shaped conjugate strike-slip faults and the corresponding continuum mode of continental deformation. *Geol. Soc. Am. Bull.* 123 (9-10), 1798–1821. doi:10.1130/B30159.1

York, D. (1968). Least squares fitting of a straight line with correlated errors. *Earth Planet. Sci. Lett.* 5, 320–324. doi:10.1016/S0012-821X(68)80059-7

Zhao, Q., Yan, Y., Tonai, S., Tomioka, N., Clift, P. D., Hassan, M. H. A., et al. (2022). A new K-Ar illite dating application to constrain the timing of subduction in West Sarawak, Borneo. *Geol. Soc. Am. Bull.* 134 (1-2), 405–418. doi:10.1130/B35895.1

Zheng, Y., Kong, P., and Fu, Bi. (2014). Time constraints on the emplacement of klippen in the longmen Shan thrust belt and tectonic implications. *Tectonophysics* 634 (6), 44–54. doi:10.1016/j.tecto.2014.07.018

Zheng, Y., Li, H., Sun, Z., Wang, H., Zhang, J., Li, C., et al. (2016). New geochronology constraints on timing and depth of the ancient earthquakes along the Longmen Shan fault belt, eastern Tibet. *Tectonics* 35 (12), 2781–2806. doi:10.1002/2016TC004210

Zuo, J., Wu, Z., Ha, G., Hu, M., Zhou, C., and Gai, H. (2021). Spatial variation of nearly NS-trending normal faulting in the southern Yadong-Gulu rift, Tibet: New constraints from the Chongba Yumtso fault, Duoqing Co graben. *J. Struct. Geol.* 144, 104256. doi:10.1016/j.jsg.2020.104256

Zwingmann, H., and Mancktelow, N. (2004). Timing of Alpine fault gouges. *Earth Planet. Sci. Lett.* 223 (3-4), 415–425. doi:10.1016/j.epsl.2004.04.041